PHYSICAL REVIEW B **110**, 085406 (2024)

Two-dimensional electron gas on the surface of alkali-earth metal based electrides: Assistance to overcome tunneling barriers in ohmic contacts

Chengfeng Pan,[1,2] Anqi Shi,[1] Xiuyun Zhang,[3] Yu-Ning Wu,[2,*] Yongtao Li,[1,†] and Xianghong Niu[1,4,‡]

[1] *State Key Laboratory of Organic Electronics and Information Displays and Institute of Advanced Materials (IAM), School of Science, Nanjing University of Posts and Telecommunications, Nanjing 210023, China*

[2] *Key Laboratory of Polar Materials and Devices (MOE), and Department of Electronics, East China Normal University, Shanghai 200241, China*

[3] *College of Physics Science and Technology, Yangzhou University, Yangzhou 225002, China*

[4] *Key Laboratory of Quantum Materials and Devices (Southeast University), Ministry of Education, Nanjing 211189, China*

(Received 8 May 2024; revised 6 July 2024; accepted 19 July 2024; published 5 August 2024)

van der Waals (vdW) stacking of two-dimensional (2D) metals and 2D semiconductors has attracted significant interest in metal-semiconductor junctions (MSJs). Unfortunately, the vdW gap always leads to large tunneling barriers even in ohmic contacts. Herein, by constructing 2D electrides possessing sufficient electron gas at the surface, the formation of quasibonds at MSJ interface is expected to overcome the challenge of contact resistance induced by vdW gap. Specifically, 2D Ca_2XY_2 (X = Ti, Zr, Hf; Y = N, P) electrides possess ultralow work functions ranging from 3.28 to 3.90 eV, accompanied by nearly free electrons on the surface, rendering them efficient electron donors. Taking typical 2D semiconductor MoS_2 to contact Ca_2XY_2, the ohmic contact and complete tunneling effect can be achieved. Application of a modest bias voltage yields a noticeable current density of about 0.6 $\mu A/Å^2$. Moreover, these MSJs exhibit superior environmental stability with bromine terminated. Our work not only offers a series of promising 2D electrides, but also paves the way for advancing the progress of 2D electronic and optoelectronic devices.

DOI: 10.1103/PhysRevB.110.085406

I. INTRODUCTION

With the increasing demand for miniaturization of devices, two-dimensional (2D) metals provide a promising platform for developing nanoscale electronic devices [1–4]. As the crucial components of electronic and photoelectronic devices, metal-semiconductor junctions (MSJs) with ohmic contacts are essential to the device's performance. Compared with the bulk metals, 2D metals lack dangling bonds on the surface, which interact with 2D semiconductors via van der Waals (vdW) forces, significantly suppressing the chemical disorder and releasing the lattice mismatch. This largely avoids metal-induced gap states and disorderly induced gap states. Therefore, the Fermi-level pinning effect is weak and the Schottky-Mott limit can be approached in 2D MSJs [5–9]. However, the intrinsic vdW gap leads to a large tunneling barrier, limiting the tunneling probability [10,11]. In previous studies, transition-metal dichalcogenides AB_2 (A = Nb, Ta; B = S, Se), MXenes, graphene, germanene, etc., have been utilized as electrodes in 2D MSJs [12–17]. Although some approaches such as hydrogenated interface [18] and polarization reversal [19,20] have been employed to meet the above two requirements, these strategies are not satisfactory and bring inconvenience in practical operation. Therefore, it is urgent to explore high-effect contact modes for overcoming vdW gap in 2D ohmic contacts.

Interestingly, the intrinsic features of 2D electrides, such as Ca_2N [21], provide a potential platform for highly efficient carrier injection/extraction. On the one hand, 2D electrides possess ultralow work functions, facilitating the formation of ohmic contacts. On the other hand, freely diffused anionic electrons, that is, free 2D electron gas [22,23], make them effective electron donators. For example, the interface of 2D Ca_2N and ZrS_2 dominates by the quasibond interaction, and the vdW gap can be filled with the massive free electrons [24]. Inserting 2D Ca_2N between MoS_2 and bulk Au can effectively eliminate both the tunneling and Schottky barriers due to the charge transfer from the surface of Ca_2N [25]. However, harnessing these exceptional properties to improve contact characteristics in 2D MSJs is also accompanied with certain drawbacks. For example, the environmental instability of Ca_2N presents a significant obstacle to further development [26]. Up to now, except 2D Ca_2N and its derivatives predicted as M_2K (M = Ca, Sr, Ba; K = N, P, As, Sb) [27], obtaining workable 2D electrides still faces significant challenges to high-performance 2D MSJs.

Herein, enlightened by $P_{n+1}Q_n$ configurations of MXenes ($n = 1, 2\ldots$) [28], rearranging atomic layers of existing 2D electrides may have great potential to improve the performance of 2D MSJs. Through redesigning the atomic layer arrangement of 2D Ca_2N, the layers' arrangement from top to bottom is set as Ca-Y-X-Y-Ca (X = Ti, Zr, Hf; Y = N, P). Then, 2D Ca_2XY_2 electrides obtained possess ultralow work functions ranging from 3.28 to 3.90 eV and nearly

---

[*] Contact author: ynwu@phy.ecnu.edu.cn

[†] Contact author: liyt@njupt.edu.cn

[‡] Contact author: xhniu@njupt.edu.cn

2469-9950/2024/110(8)/085406(10)

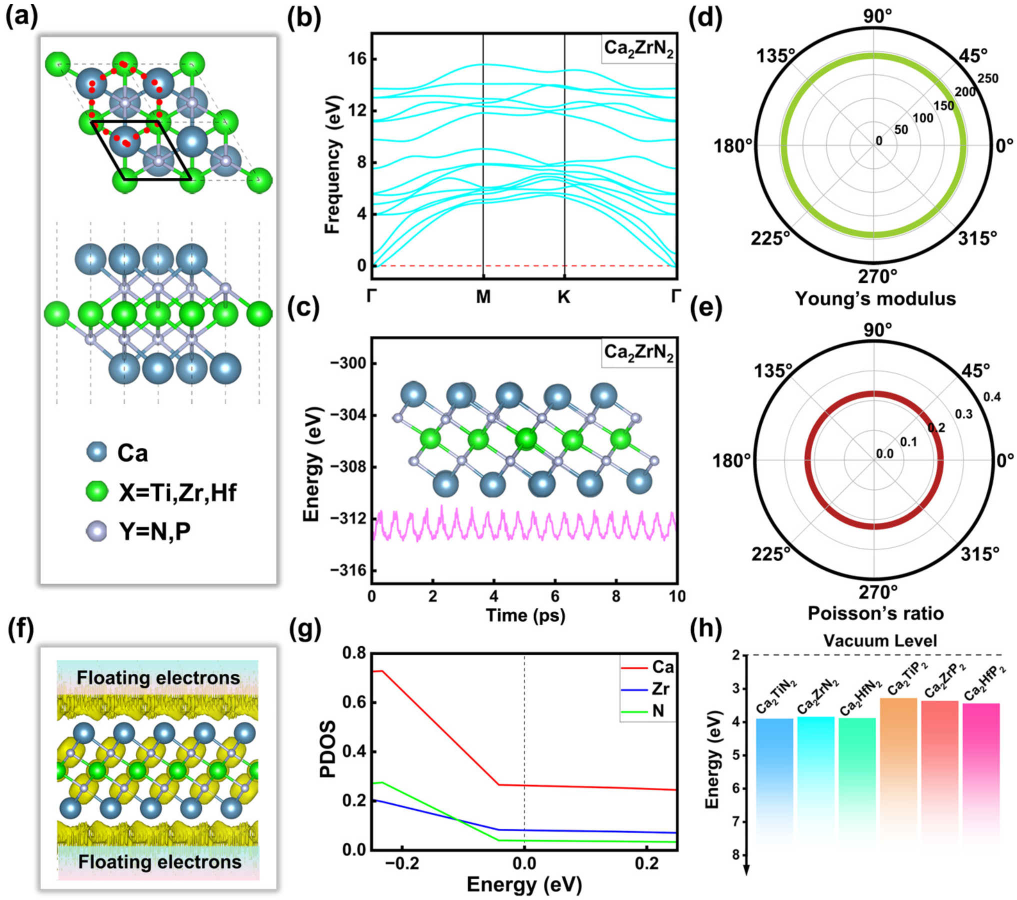

FIG. 1. (a) Top and side views of 2D Ca_2XY_2. (b) The phonon spectrum of 2D Ca_2ZrN_2. (c) Energy fluctuation from AIMD simulations for 2D Ca_2ZrN_2 at 300 K. Insets show the simulation's snapshot after 10 ps. In-plane (d) Young's modulus and (e) Poisson's ratio for 2D Ca_2ZrN_2 as a function of angle θ. (f) ELF of 2D Ca_2ZrN_2. (g) PDOS of 2D Ca_2ZrN_2; the red, blue, and green lines represent the contributions of Ca, Zr and N atoms, respectively. (h) Work functions of 2D Ca_2XY_2.

free 2D electrons gas on the surface, making them effective electron donators. Given the significance of MoS_2 in the field of 2D semiconductors, we employ 2*H*-MoS_2 to interface with 2D Ca_2XY_2, unveiling their contact properties. Excitingly, all MoS_2/Ca_2XY_2 junctions exhibit ohmic contacts with a 100% tunneling probability, and structural stability can be maintained through *ab initio* molecular dynamics (AIMD) simulations. The transmission spectra and *I*-*V* curves demonstrate the excellent transport properties of MoS_2/Ca_2HfY_2 junctions. Additionally, bromination treatment on the uncontacted surface remarkably enhances the device's stability in the air.

II. COMPUTATIONAL METHODS

First-principles calculations were performed with the Vienna *Ab initio* Simulation Package (VASP) under the framework of the Perdew-Burke-Ernzerhof functional and the generalized gradient approximation [29–31]. The energy cutoff for plane-wave basis was set to 450 eV. The convergence criteria of electron and ion relaxation were set as 10^{-6} eV per atom and 0.01 eV/Å, respectively. The k-point sampling in the Brillouin zone was performed by employing the Monkhorst-Pack k-point meshes of $10\times10\times1$ [32]. To eliminate the interactions between adjacent layers, a vacuum space of more than 15 Å along the z direction was adopted. DFT-D3 method of Grimme with zero-damping function was used to describe van der Waals interactions [33]. Phonon dispersion spectrums were calculated with the $4 \times 4 \times 1$ supercell by the PHONOPY code within the density-functional perturbation theory to evaluate the dynamical stability [34,35]. Thermodynamic stability was checked via AIMD by the Nosé thermostat method in the *NVT* ensemble at 300 K [36,37]. The simulation time was 10 ps with a time step of 1 fs. Bader analysis was performed to evaluate the number of charge transfers [38]. To match the lattice constant between Ca_2XY_2 and MoS_2 as much as possible, the $1 \times 1 \times 1$ Ca_2XN_2 and $1 \times 1 \times 1$ MoS_2 and $\sqrt{3} \times \sqrt{3} \times 1Ca_2XP_2$ and $2 \times 2 \times 1$ MoS_2 supercell were adopted. The lattice constant mismatching rate was controlled within 5% (cf. Table S2 in the Supplemental Material (SM) [39]). Integrating local density of states (ILDOS) was utilized to visualize the surface states in real space:

$$Q(\boldsymbol{r}) = \int_{E_0}^{E_F} \sum_{\{k\},n} |\Psi(r,E)|^2 \delta(E - E_{\{k\},n}) dE, \qquad (1)$$

in which E_F, E_0, n, and $E_{\{k\},n}$ represent the Fermi level, bottom edge of the surface band, band index, and eigenenergies, respectively. An example of surface band is the band branches highlighted in bold sky-blue lines near the Fermi level [see

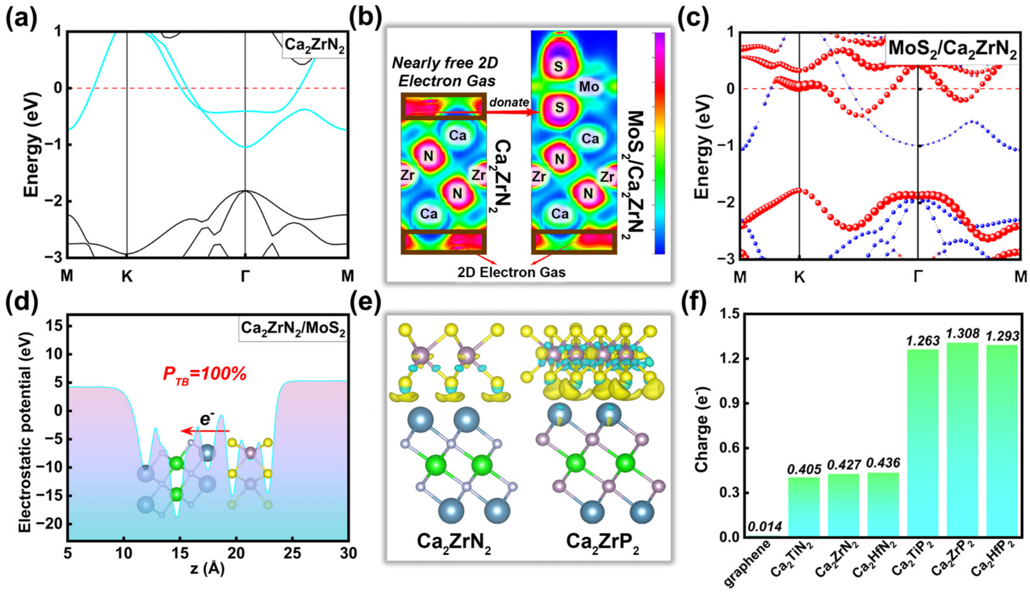

FIG. 2. (a) The band structure of 2D Ca_2ZrN_2 in the M-K-Γ-M path, and the Fermi level is set to zero. (b) ELF of 2D Ca_2ZrN_2 and MoS_2/Ca_2ZrN_2 junction. (c) The projected band structure of MoS_2/Ca_2ZrN_2 junction with the Fermi level set to zero. The red and blue dots represent the contributions of MoS_2 and Ca_2ZrN_2, respectively. (d) The electrostatic potential of MoS_2/Ca_2ZrN_2 junction. (e) Plane-averaged charge-density difference between MoS_2 and Ca_2ZrY_2. (isovalue: 0.004 e/Å-3; yellow: electron accumulation; blue: electron depletion) (f) Quantity of electrons transfer from Ca_2XY_2 (graphene) to MoS_2 layer.

Fig. 2(a)]. By integrating the planar average of ILDOS, $Q(z)$ from the Ca atoms to the vacuum region, the surface charges (Q_{SC}) of 2D Ca_2XY_2 can be evaluated as

$$Q_{\mathrm{SC}} = \int_{z1}^{z2} Q(z)dz, \tag{2}$$

where $z1$ and $z2$ represent the position of the Ca atoms and the vacuum region, respectively.

The quantum transport properties of MoS_2/Ca_2HfY_2 junctions were calculated by using nonequilibrium Green's function in the NANODCAL package [40]. The convergence criterion of density matrix was set as 10^{-6} hartree and a $1 \times 9 \times 1$ k-point mesh was employed to perform the self-consistent calculations. A $1 \times 100 \times 1$ k-point mesh was used to calculate the current-voltage curve and transmission spectrum for the central region. The transmission coefficient was calculated by the following formula:

$$T(E) = \mathrm{Tr}[\Gamma_L(E)G^r(E)\Gamma_R(E)G^a(E)], \tag{3}$$

where Γ_L and Γ_R represent a linewidth function for describing the coupling between the channel and electrode. The advanced Green function G^a is the Hermitian conjugate of the retarded Green function G^r. The electric current is determined by the Landauer-Buttiker formula [41]:

$$I(V_b) = \int_{-\frac{V_b}{2}}^{\frac{V_b}{2}} I(E)dE = -\frac{2q}{h}\int_{-\frac{V_b}{2}}^{\frac{V_b}{2}} T(E)[f_L(E, V_L) - f_R(E, V_R)]dE, \tag{4}$$

where $I(E)$ refers to the spectral current, and $T(E)$ is the transmission coefficient under external bias voltage $V_b = V_L - V_R$ in which V_L and V_R represents the potential of the left and right electrodes, and f_L/f_R is the Fermi-Dirac distribution function of the left/right electrodes.

III. RESULTS AND DISCUSSION

A. Geometric structures of 2D Ca_2XY_2

The crystal structure of 2D Ca_2XY_2 is shown in Fig. 1(a), in which the Y atoms are located as the central layer of Ca and X layers with strong bonding to make structures stable. The red dotted lines underline the region of cavity composed of Ca and X cations, satisfying the basic rule for electrides, namely, the metallic atoms comprising the coordination around the anionic electrons must exhibit electropositive characteristics [42]. The lattice constants of 2D Ca_2XY_2 range from 3.23 to 3.88 Å, comparable to the lattice constant of 2D Ca_2N (3.57 Å) [43]. Additionally, bond length of Ca–N is 2.42 Å in 2D Ca_2N, which barely alters in 2D Ca_2XN_2 (cf. Table I), although the bond length of Ca–P becomes larger due to the smaller ionic radius of N^{3-} compared to P^{3-} [44], which is also comparable to the Ca–N bond length. Hence, this design strategy does not cause significant lattice variation, which is favorable to the structural stability. In the SM [39], Fig. S1 shows the x-ray-diffraction (XRD) patterns of 2D Ca_2XY_2, providing the reference for the future experimental synthesis.

B. Stability of 2D Ca_2XY_2

The cohesive energy serves as a thermodynamic foundation for the robust stability of 2D Ca_2XY_2, which can be defined as

$$E_{\mathrm{co}} = \frac{2E_{\mathrm{Ca}} + E_X + 2E_Y - E_{\mathrm{Ca}_2XY_2}}{5}, \tag{5}$$

where $E_{\mathrm{Ca}_2XY_2}$, E_{Ca}, E_X, and E_Y are the total energies of Ca_2XY_2, single Ca, X, and Y atoms, respectively. The cohesive energies of Ca_2XN_2 and Ca_2XP_2 are about 5 and 3 eV per atom, respectively (cf. Table I). These values are

TABLE I. The lattice constants, bond lengths, cohesive energies, work functions, and Young's modules of 2D Ca_2XY_2.

2D electrides	Lattice constant (Å)	Ca-Y bond length (Å)	X-Y bond length (Å)	Cohesive energy (eV per atom)	Work function (eV)	Young's modulus (N/m)
Ca_2TiN_2	3.230	2.338	2.200	4.859	3.895	164.106
Ca_2ZrN_2	3.330	2.400	2.299	4.907	3.837	190.273
Ca_2HfN_2	3.310	2.411	2.270	5.022	3.877	199.680
Ca_2TiP_2	3.790	2.745	2.568	2.840	3.279	82.240
Ca_2ZrP_2	3.880	2.759	2.694	2.894	3.359	92.264
Ca_2HfP_2	3.840	2.760	2.658	2.941	3.438	93.573

comparable with MoS_2's (4.89 eV per atom) and silicene's (3.91 eV per atom) [45,46], implying the strongly bonded networks. Compared with 2D Ca_2XP_2, the larger cohesive energies of Ca_2XN_2 reflect the stronger interactions between atoms, which is consistent with the smaller bond lengths in 2D Ca_2XN_2. The dynamics and thermodynamics stabilities further support the feasibility of the experimental synthesis. In the phonon dispersion of 2D Ca_2XY_2, the absence of imaginary frequency indicates the dynamical stability (see Figs. 1(b) and S2 in the SM [39]). For 2D Ca_2XP_2, their larger bond lengths mean the looser interaction with the neighboring atoms, explaining the flatness of the highest phonon mode in the high-energy region [47]. During the AIMD simulations, the energy oscillates around the equilibrium state and any structural reorganization is invisible (see Figs. 1(c) and S3 in the SM [39]).

Under the Born criteria [48], namely $C_{11} > C_{12}$ and $C_{11},\ C_{22},\ C_{66} > 0$, the mechanical stability of 2D Ca_2XY_2 is confirmed. Due to hexagonal symmetry, elastic constants C_{11} equal to C_{22}, and C_{66} can be written as $\frac{C_{11}-C_{12}}{2}$. Thus, 2D Ca_2XY_2 is mechanically stable (cf. Table S1 in the SM [39]). Further, Young's modulus $Y(\theta)$ and Poisson's ratio $\upsilon(\theta)$ of 2D Ca_2XY_2 can be obtained as follows [49]:

$$Y(\theta) = \frac{C_{11}C_{22} - {C_{12}}^2}{C_{11}\sin^4\theta + A\sin^2\theta\cos^2\theta + C_{22}\cos^4\theta}, \tag{6}$$

$$\upsilon(\theta) = \frac{C_{12}\sin^4\theta - B\sin^2\theta\cos^2\theta C_{22} + C_{12}\cos^4\theta}{C_{11}\sin^4\theta + A\sin^2\theta\cos^2\theta + C_{22}\cos^4\theta}, \tag{7}$$

where $A = \frac{C_{11}C_{22}-{C_{12}}^2}{C_{66}} - 2C_{12}$, and $B = C_{11} + C_{12} - \frac{C_{11}C_{22}-{C_{12}}^2}{C_{66}}$. All these 2D Ca_2XY_2 show large Young's modulus and strong mechanical isotropy (see Figs. 1(d) and S4 in the SM [39]). As illustrated in Figs. 1(e) and S5 [39], Poisson's ratio of 2D Ca_2XY_2 is also isotropic, indicating their compressibility. The specific data are summarized in Table S1 [39]. These good intrinsic features establish a foundation for the application in 2D MSJs.

C. Electronic structures of 2D Ca_2XY_2

Before exploring 2D Ca_2XY_2-based MSJs, it is essential to establish a primary understanding of the electronic structures of 2D Ca_2XY_2. Using 2D Ca_2ZrN_2 as an illustration, electron-localization function (ELF) reveals that massive electrons are floating on the surface [see Fig. 1(f)], aligning with the behavior observed in typical electrides such as 2D Ca_2N [50]. As shown in Fig. 1(g), through the analysis of projected density of states (PDOS), the dominating contribution of states near the Fermi level comes from Ca elements, facilitating electrons to escape to the vacuum level easily. Further, using ILDOS, we evaluate the Q_{SC} for 2D Ca_2XY_2. For 2D Ca_2N, its Q_{SC} we calculated is $3.74 \times 10^{14}\ e^-\ cm^{-2}$, which is in agreement with the existing result $3.72 \times 10^{14}\ e^-\ cm^{-2}$ [51]. Figure S6 in the SM [39] shows the planar-averaged ILDOS of 2D Ca_2XY_2, their charge distribution in real space, and the specified values of Q_{SC}. As the atomic number of X increases, its peak intensity also gradually decreases, which is similar to the trend of ILDOS for M_2K [51]. Taking 2D Ca_2ZrN_2 and Ca_2HfN_2 as examples, according to PDOS (see Fig. S7 in the SM [39]), the state contributed by Zr/Hf (Ca) is weak (strong), corresponding to the valley (peak) in their planar-averaged ILPOS. Thus, the difference of Q_{SC} for 2D Ca_2XY_2 should be attributed to the different lattice constants and the ability of X to bind electrons. All 2D Ca_2XY_2 can exhibit ultralow work functions, ranging from 3.28 to 3.90 eV [see Fig. 1(h)]. Meanwhile, the fine metallicity of 2D Ca_2XY_2 ensures them to serve effectively as an electrode for interfacing with 2D semiconductors (see Fig. S8 in the SM [39]). Therefore, in the 2D Ca_2XY_2-based interfaces, accompanied with the vdW gap filled by plentiful electrons, the tunneling barriers have a chance to be eliminated in ohmic contacts.

D. Contact properties of MoS_2/Ca_2XY_2 junctions

A typical feature of 2D electrides is the nearly free 2D electron gas on the surface. Taking 2D Ca_2ZrN_2 as an example, its band branches highlighted in bold sky-blue lines exhibit a parabolic pocket near the Fermi level, deemed as characteristic of electrides [see Fig. 2(a)] [50,52,53]. In the left panel of Fig. 2(b), 2D electron gas emerges on the surface of 2D Ca_2ZrN_2, rendering it an effective electron donator. Due to the importance of MoS_2 in the field of MSJs [54], we choose $2H$-MoS_2 to contact with 2D Ca_2XY_2 for further exploration. As depicted in Fig. 2(b), when 2D Ca_2ZrN_2 contacts with MoS_2, 2D electron gas is readily transferred to the MoS_2 layer, thereby significantly impacting the electron density of MoS_2. The Fermi level enters the conduction band of MoS_2, indicating the formation of ohmic contacts (see Figs. 2(c) and S9 in the SM [39]). In addition, compared with 2D Ca_2XN_2-based MSJs, the band structure of MoS_2 undergoes a more significant alteration in MoS_2/Ca_2XP_2 MSJs. To clearly understand this behavior, taking MoS_2/Ca_2XP_2 MSJ as an example, we compare the band structures of isolated MoS_2 before and after contact. As shown in Fig. S10 [39], before and after contact, the band structure of Ca_2HfP_2 almost has no variation. Upon formation of the interface, two band branches are introduced to the gap of isolated MoS_2_contact compared to the original band gap of isolated MoS_2_no contact. It is well known that states in MoS_2 close to the Fermi level are contributed by Mo instead of S atoms. However, charge density of these two bands is distributed not only on Mo, but also partially on S atoms. Thus, the slight structure distortion caused by enhanced interlayer interaction effectively reduces conduction-band minimum, and thus induces the formation of ohmic contact. The similar phenomenon can be observed in MoS_2/Ca_2N systems [55]. Note that in order to avoid affecting the intrinsic properties of MoS_2, it is reasonable to stretch 2D Ca_2XY_2 in a small scale to match MoS_2 [56–58]. Figure S11 in the SM [39] exhibits the band structures of 2D Ca_2XY_2 under biaxial strain from −6 to 6%. Although partial band branches slightly alter, the metallicity of 2D Ca_2XY_2 remains fine and the pocketlike structures across the Fermi level do not change; thus, 2D electron gas cannot be affected by little strain.

Referring to the electrostatic potential profile depicted in Fig. 2(d), electrons can transport from the surface of MoS_2 to 2D Ca_2XY_2 without energy loss. The tunneling probability is defined as

$$P_{TB} = \exp\left(-\frac{2W_{TB}}{\hbar}\sqrt{2m\phi_{TB}}\right), \tag{8}$$

where $\hbar$, m, W_{TB}, and ϕ_{TB} represent the reduced Planck constant, the mass of the free electron, and the width and height of the tunneling barriers (TB), respectively. According to Eq. (8), a square potential has been assumed to simplify the irregular barriers into square barriers, and the P_{TB} of all MoS_2/Ca_2XY_2 junctions is 100% (see Fig. S12 in the SM [39]). In detail, the MoS_2 obtains abundant electrons from 2D electron gas, forming a robust negative space-charge region on its surface. Subsequently, the complete tunneling effect can be achieved at the MoS_2-Ca_2XY_2 interfaces. Furthermore, according to Simmon's model under the square-barrier approximation, tunneling-specific resistivity (ρ_t) can be calculated as [59,60]

$$\rho_t \approx \frac{4\pi^2\hbar W_{TB}^2}{q^2}\,\frac{\exp\left(\frac{2(2m)^{1/2}}{\hbar}W_{TB}\phi_{TB}^{1/2}\right)}{\frac{(2m)^{1/2}}{\hbar}W_{TB}\phi_{TB}^{1/2}-1}. \tag{9}$$

When W_{TB} is extremely close to zero, this equation will cause an unphysical negative value. Based on the low-bias approximation, the corrective equation is provided as follows:

$$\rho_t^* \approx \frac{8\pi^2\hbar W_{TB}}{3q^2(3m\phi_{TB})^{1.2}}\exp\left(\frac{2W_{TB}(2m\phi_{TB})^{1/2}}{\hbar}\right). \tag{10}$$

Since the value of W_{TB} is zero, $\rho_t^* \approx 0$, which is much smaller than that in LSi_2N_4-2D (3D) metals contacts ($L =$ Mo, W) [61,62]. Moreover, the interface charge redistribution between MoS_2 and Ca_2ZrY_2 can be demonstrated by the charge-density differences, which can be defined as

$$\Delta\rho = \rho_{MSJ} - \rho_{Ca_2ZrY_2} - \rho_{MoS_2}, \tag{11}$$

where ρ_{MSJ}, $\rho_{Ca_2ZrY_2}$, and ρ_{MoS_2} represent the charge densities of the 2D MSJ, Ca_2ZrY_2,and MoS_2, respectively. Regardless of whether they are N- or P-based electrides, the strength of charge rearrangement is remarkable [see Fig. 2(e)], which can be attributed to the large difference in work functions between MoS_2 and Ca_2ZrY_2. In addition, Bader analysis indicates that the quantity of charges donated from 2D Ca_2XY_2 to MoS_2 significantly exceeds that observed in the graphene-MoS_2 contact [see Fig. 2(f)]. This behavior, different from the common 2D vdW system, implies the stronger interlayer interactions. Under this stronger coupling mode, the elimination of the tunneling barriers induced by the vdW gap is entirely comprehensible.

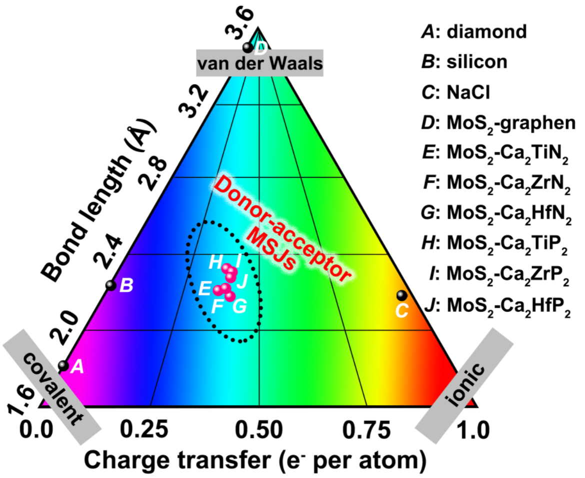

FIG. 3. Bond length of covalent, ionic, and vdW systems. The black balls represent some well-known examples such as diamond–silicon having no net electron transfer, typical ionic crystal NaCl, and the common MoS_2/graphene vdW junction. The pink balls gives the information of bonding and charge transfer in MoS_2/Ca_2XY_2 junctions. Here, charge transfer refers to the transfer from each Ca to MoS_2 layer.

E. Quasibond in donor-acceptor MSJs

In fact, the concept of quasibond provides a clearer understanding of this stronger coupling mode. Compared to the vdW forces, the systems dominated by quasibond show the shorter bonding distance and denser charge transfer [63,64]. As shown in Fig. 3, we choose 3.6 (1.6) Å as the bonding length to represent vdW (covalent) interaction, and the ultimate charge transfer in ionic bonding is $1\,e^-$. Within this framework, MoS_2/Ca_2XY_2 systems are mainly concentrated in the central area of the "triangle," behaving as the typical donor-acceptor MSJs. Specifically, in these donor-acceptor MSJs, the quasibond interaction causes the slight structural distortion of MoS_2 (more apparent in MoS_2-Ca_2XP_2 contacts; see Fig. S13 in the SM [39]), thus further inducing the overlapped states [24]. Then, the moderately enhanced charge redistribution can effectively promote the contact properties. By introducing the concept of quasibond, it is clear that strengthened interlayer interaction is the key to eliminating vdW gap in 2D ohmic contacts.

With stronger interlayer interactions and enhanced charge transfer, the phenomenon of reconstruction may occur in 2D thin-layer structures. For example, 2D Ca_2EN_2 ($E =$ Zr,

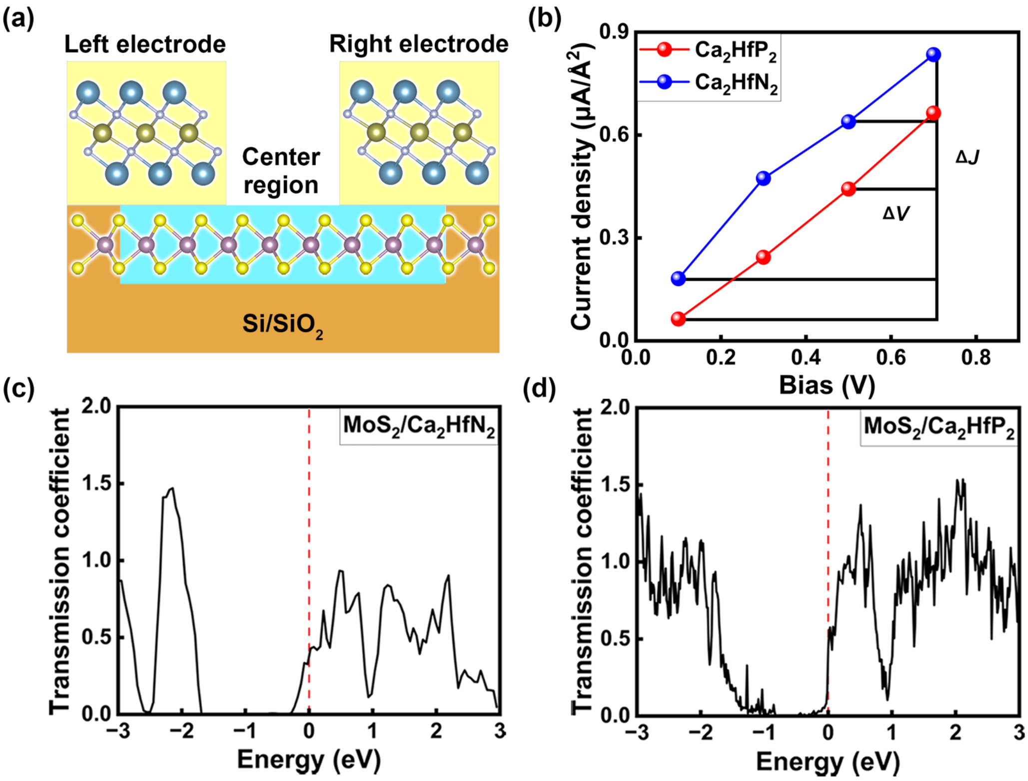

FIG. 4. (a) Schematic of a two-probe model of MoS_2/Ca_2HfN_2 junction. (b) The current-density–voltage curves for MoS_2/Ca_2HfN_2 and MoS_2/Ca_2HfP_2 junctions. The transmission spectra with zero bias of (c) MoS_2/Ca_2HfN_2 and (d) MoS_2/Ca_2HfP_2 junctions. The Fermi level is set to zero.

Hf) can effectively decrease the phase-transition barrier for $2H$-$MoTe_2$ and stabilizes the $1T'$ phase. This phenomenon can be mainly attributed to the synergistic effect of the ultralow-energy difference (about 0.043 eV) between $2H$ and $1T'$-$MoTe_2$ [65], as well as nearly free 2D electron gas on the surface. For MoS_2, a large phase-transition energy of about 0.55 eV hardly allows similar behavior to be observed [66]. To confirm the structural collapse and phase transition do not exist in the MoS_2/Ca_2XY_2 systems, AIMD simulations are performed at 300 K for 10 ps. As shown in Fig. S14 [39], the energies smoothly fluctuate in a small range, and the structures of these 2D MSJs have no significant distortion or breakdown. The charge transfer from 2D Ca_2XY_2 to MoS_2 is not sufficient to cause a phase transition. This point is in line with our original purpose of designing such electrides that can be utilized to realize stable and high-performance 2D MSJs.

F. Transport properties of MoS_2/Ca_2HfY_2 junctions

Furthermore, we take MoS_2/Ca_2HfY_2 junctions as instances to simulate their transport characteristics using the common two-probe model [see Fig. 4(a)]. In Figs. 4(c) and 4(d), the transmission spectra clearly show the ohmic contacts in MoS_2/Ca_2HfY_2 junctions. The transmission states crossed by the Fermi level allow the effective electron tunneling to form considerable interfacial currents. Figure 4(b) shows the roughly linear curves, and the current densities rapidly increase with the bias voltage added from 0.1 to 0.7 V, which are typical features distinguished from Schottky contact. For nanoscale electronic devices, the impact of heating on their performance is also crucial [67]. Generally, the generated heat is proportional to the resistance. Resistance per unit area can be evaluated from I-V curves via the following equation:

$$R_s = \frac{\Delta V}{\Delta J}, \tag{12}$$

where V and J are voltage and current density, respectively. R_s of MoS_2/Ca_2HfN_2 and MoS_2/Ca_2HfP_2 junctions are 1.022 and 0.902 $\text{Å}^2\text{V}/\mu\text{A}$, implying less heat loss in the MoS_2/Ca_2HfP_2 junction. Thus, compared with 2D Ca_2HfN_2, 2D Ca_2HfP_2 is the better potential candidate for the design of electronic devices based on MoS_2.

G. Bromination of MoS_2/Ca_2HfP_2 junctions

Like other electrides, the oxidation and hydrolysis also hinder the practical application of 2D Ca_2XY_2. The remaining 2D electron gas on the noncontact side can easily induce the chemical adsorption of oxygen (O_2) and water (H_2O) molecules in the air. Taking MoS_2/Ca_2HfP_2 as an example, the adsorption energies indicate that O_2 and H_2O can be adsorbed chemically on the 2D Ca_2HfP_2 [see Fig. 5(a)]. Thus, an appropriate surface modification is necessary to stabilize the performance of devices. Halogenation on the surface of 2D materials has been considered an effective approach for modification [68,69]. Here, we employ bromination treatment to prevent the disintegration. Note that bromine-terminated surface will not remarkably alter the electronic structures,

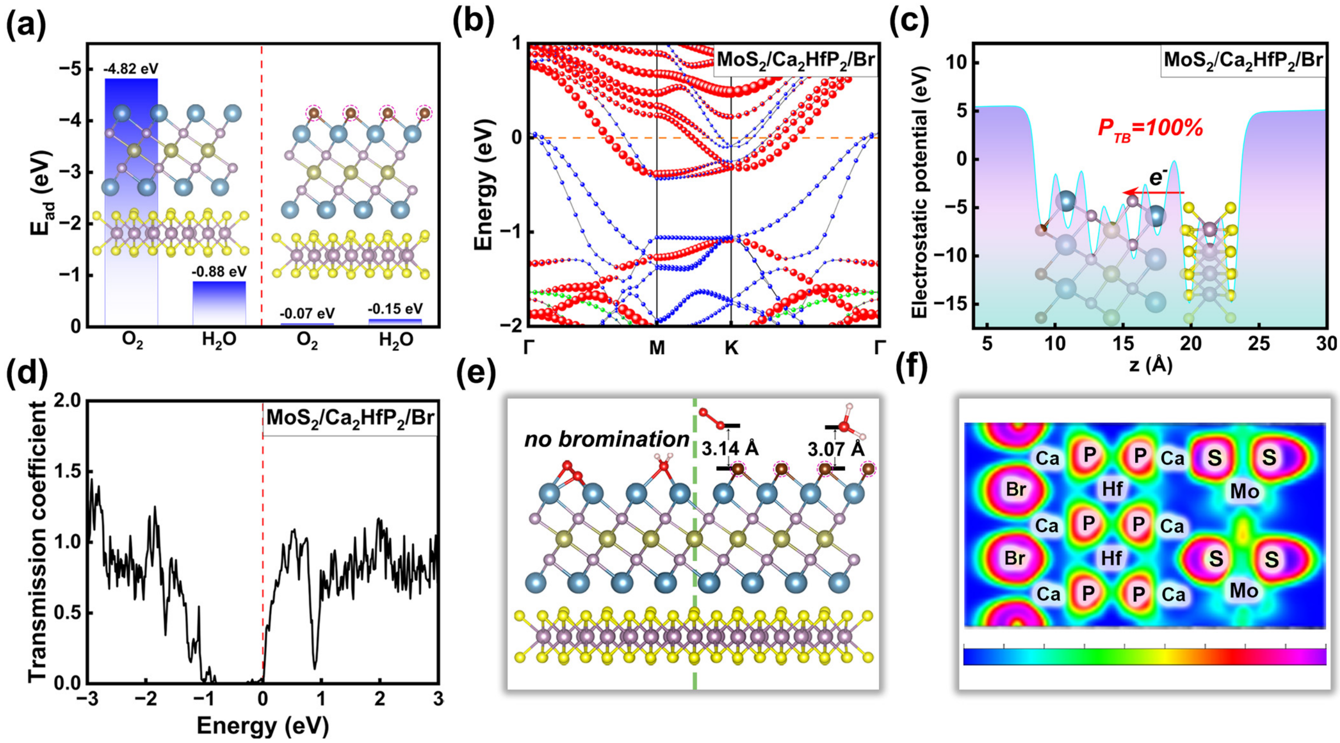

FIG. 5. (a) Adsorption energies of O_2 and H_2O for MoS_2/Ca_2HfP_2 (left panel) and $MoS_2/Ca_2HfP_2/Br$ (right panel) junctions. (b) The projected band structure of $MoS_2/Ca_2HfP_2/Br$ junction, and the Fermi level is set to zero. The red, blue, and green dots represent the contributions of MoS_2 Ca_2HfP_2, and Br, respectively. (c) The transmission spectrum with zero bias, (d) electrostatic potential, and (f) ELF of $MoS_2/Ca_2HfP_2/Br$ junction. (e) Optimized structures of MoS_2/Ca_2HfP_2 and $MoS_2/Ca_2HfP_2/Br$ junctions when O_2 and H_2O float on the surface.

which can be illustrated by comparing band structures in Figs. 5(b) and S8(f). The contribution of Br to the band is slight and is mainly reflected in the energy region of −2 eV, implying the little impact on the contact properties. As shown in Fig. 5(c), electrons transfer from MoS_2 to Ca_2HfP_2/Br without being hindered by tunneling barriers, implying that the filling of the vdW gap by massive electrons remains unaffected. Moreover, the transmission spectrum also indicates that the complete tunneling effect at the interface is uncompromised [see Fig. 5(d)]. Hence, the influence of additional Br on the electrical performance of devices can be disregarded.

On the brominated surface, O_2 and H_2O can only be adsorbed physically due to the protection of Br atoms layer. As depicted in Fig. 5(e), the noncontact side of Ca_2HfP_2 exhibits an inclination to bond with O_2 and H_2O, while O_2 and H_2O maintain approximately 3 Å from Br atoms in $MoS_2/Ca_2HfP_2/Br$ junction. Moreover, ELF in Fig. 5(f) clearly illustrates that Br atoms can deplete the 2D electron gas on the non-contact surface, elucidating why O_2 and H_2O no longer strongly bond with Ca_2HfP_2. Importantly, the AIMD simulation not only verifies the stability of $MoS_2/Ca_2HfP_2/Br$ junction (see Fig. S15 in the SM [39]), but also demonstrates the dynamical isolation effect of O_2 and H_2O. The snapshots of the simulation for 2, 4, 6, and 8 ps can be searched in Fig. S16 [39], in which H_2O throughout keeps about 3 Å away from the brominated interface while O_2 is repelled. This phenomenon is also in line with the fact that the adsorption energy of O_2 is almost zero, while that of H_2O is −0.15 eV. This case of the surface modification allowing the device to be environmentally stable should also be practical for other 2D electrides.

IV. CONCLUSIONS

In summary, through redesigning atomic layers arrangement, we obtain a series of 2D Ca_2XY_2 from the source material Ca_2N. These 2D Ca_2XY_2 not only behave steadily in dynamics and thermodynamics, but also possess typical electride properties. Since the bifunctional effect of the ultralow work functions and 2D electron gas on the surface, ohmic contacts can be formed in MoS_2-Ca_2XY_2 interfaces with the full tunneling effect. With a small bias voltage applied to the MoS_2/Ca_2HfY_2 junctions, the notable currents observed suggest the absence of Schottky barriers. Furthermore, the brominated surface serves as an effective barrier against hydrolysis and oxidation, and the excellent contact characteristics previously demonstrated are almost uncompromised. These findings provide a feasible case to design 2D electrides on the existing basis and stimulate more interest in eliminating vdWs gap in 2D MSJs.

ACKNOWLEDGMENTS

This work is supported by the China Postdoctoral Science Foundation (Grant No. 2022M711691), Six talent peaks project in Jiangsu Province (Grant No. XCL-104), the open research fund of Key Laboratory of Quantum Materials and

Devices (Southeast University), Ministry of Education (Grant No. 3207022401C3) and Natural Science Foundation of Nanjing University of Posts and Telecommunications (Grant No. NY221102).

[1] S. Das, A. Sebastian, E. Pop, C. J. McClellan, A. D. Franklin, T. Grasser, T. Knobloch, Y. Illarionov, A. V. Penumatcha, J. Appenzeller *et al.*, Transistors based on two-dimensional materials for future integrated circuits, Nat. Electron. **4**, 786 (2021).

[2] Y. Wang, J. C. Kim, R. J. Wu, J. Martinez, X. Song, J. Yang, F. Zhao, A. Mkhoyan, H. Y. Jeong, and M. Chhowalla, van der Waals contacts between three-dimensional metals and two-dimensional semiconductors, Nature (London) **568**, 70 (2019).

[3] C. Tan, X. Cao, X.-J. Wu, Q. He, J. Yang, X. Zhang, J. Chen, W. Zhao, S. Han, G.-H. Nam *et al.*, Recent advances in ultrathin two-dimensional nanomaterials, Chem. Rev. **117**, 6225 (2017).

[4] Y. Chen, Z. Fan, Z. Zhang, W. Niu, C. Li, N. Yang, B. Chen, and H. Zhang, Two-dimensional metal nanomaterials: Synthesis, properties, and applications, Chem. Rev. **118**, 6409 (2018).

[5] Y. Liu, J. Guo, E. Zhu, L. Liao, S. J. Lee, M. Ding, I. Shakir, V. Gambin, Y. Huang, and X. Duan, Approaching the Schottky-Mott limit in van der Waals metal-semiconductor junctions, Nature (London) **557**, 696 (2018).

[6] Y. Liu, P. Stradins, and S. H. Wei, van der Waals metal-semiconductor junction: Weak Fermi level pinning enables effective tuning of Schottky barrier, Sci. Adv. **2**, e1600069 (2016).

[7] X. Liu, M. S. Choi, E. Hwang, W. J. Yoo, and J. Sun, Fermi level pinning dependent 2D semiconductor devices: Challenges and prospects, Adv. Mater. **34**, 2108425 (2022).

[8] S. J. Liang, B. Cheng, X. Cui, and F. Miao, van der Waals heterostructures for high-performance device applications: Challenges and opportunities, Adv. Mater. **32**, e1903800 (2020).

[9] C. Pan, A. Shi, W. Gong, W. Chen, J. Yan, X. Zhang, Z. Zhou, B. Wang, Y. Li, and X. Niu, Defected BN substrate induces the transition from Schottky to Ohmic contact in two-dimensional metals–semiconductor junctions, ACS Mater. Lett. **6**, 2118 (2024).

[10] T. Shen, J. C. Ren, X. Liu, S. Li, and W. Liu, van der Waals stacking induced transition from Schottky to Ohmic contacts: 2D metals on multilayer InSe, J. Am. Chem. Soc. **141**, 3110 (2019).

[11] Y. Hu, X. Hu, Y. Wang, C. Lu, A. V. Krasheninnikov, Z. Chen, and L. Sun, Suppressed Fermi level pinning and wide-range tunable Schottky barrier in CrX_3 ($X = \mathrm{I}$, Br)/2D metal contacts, J. Phys. Chem. Lett. **14**, 2807 (2023).

[12] X. Ding, Y. Zhao, H. Xiao, and L. Qiao, Engineering Schottky-to-Ohmic contact transition for 2D metal–semiconductor junctions, Appl. Phys. Lett. **118**, 091601 (2021).

[13] X. Yang, B. Sa, P. Lin, C. Xu, Q. Zhu, H. Zhan, and Z. Sun, Tunable contacts in graphene/InSe van der Waals heterostructures, J. Phys. Chem. C **124**, 23699 (2020).

[14] H. Zeng, R. S. Chen, and G. Yao, Tunable electronic properties and potential applications of 2D GeP/graphene van der Waals heterostructure, Adv. Electron. Mater. **6**, 1901024 (2020).

[15] N. Zhao and U. Schwingenschlogl, Transition from Schottky to Ohmic contacts in Janus MoSSe/germanene heterostructures, Nanoscale **12**, 11448 (2020).

[16] Y. Wang, H. Yuan, Z. Li, and J. Yang, Schottky and Ohmic contacts at α-Tellurene/2D metal interfaces, ACS Appl. Electron. Mater. **4**, 1082 (2022).

[17] P. T. T. Le, N. N. Hieu, L. M. Bui, H. V. Phuc, B. D. Hoi, B. Amin, and C. V. Nguyen, Structural and electronic properties of a van der Waals heterostructure based on silicene and gallium selenide: Effect of strain and electric field, Phys. Chem. Chem. Phys. **20**, 27856 (2018).

[18] D. Liu, Z. Liu, J. Zhu, and M. Zhang, Hydrogen-bonding enables two-dimensional metal/semiconductor tunable contacts approaching the quantum limit and the modified Schottky–Mott limit simultaneously, Mater. Horiz. **10**, 5621 (2023).

[19] C. Pan, W. Li, A. Shi, W. Zhang, H. Shu, F. Chi, W. Chen, X. Niu, B. Wang, and X. Zhang, Enhancing the contact performance of two-dimensional metals/In_2S_3 junctions by the self-repair of sulfur vacancies in air, ACS Appl. Electron. Mater. **5**, 4485 (2023).

[20] L. Kang, P. Jiang, H. Hao, Y. Zhou, X. Zheng, L. Zhang, and Z. Zeng, Giant tunneling electroresistance in two-dimensional ferroelectric tunnel junctions with out-of-plane ferroelectric polarization, Phys. Rev. B **101**, 014105 (2020).

[21] J. Chae and G. Kim, First-principles study of electronic and optical properties of two-dimensional Ca_2N electride using pseudoatomic orbital basis set, Phys. Rev. B **108**, 125407 (2023).

[22] C. Liu, S. A. Nikolaev, W. Ren, and L. A. Burton, Electrides: A review, J. Mater. Chem. C **8**, 10551 (2020).

[23] K. Lee, S. W. Kim, Y. Toda, S. Matsuishi, and H. Hosono, Dicalcium nitride as a two-dimensional electride with an anionic electron layer, Nature (London) **494**, 336 (2013).

[24] A. H. Woomer, D. L. Druffel, J. D. Sundberg, J. T. Pawlik, and S. C. Warren, Bonding in 2D donor–acceptor heterostructures, J. Am. Chem. Soc. **141**, 10300 (2019).

[25] F. Kaadou, J. Maassen, and E. R. Johnson, Improved charge transfer and barrier lowering across a $\mathrm{Au} - \mathrm{MoS_2}$ interface through insertion of a layered Ca_2N electride, J. Phys. Chem. C **125**, 11656 (2021).

[26] A. Walsh and D. O. Scanlon, Electron excess in alkaline earth sub-nitrides: 2D electron gas or 3D electride? J. Mater. Chem. C **1**, 3525 (2013).

[27] M. Rafiee Diznab, A. F. Rumson, J. Maassen, and E. R. Johnson, Designing barrier-free metal/MoS_2 contacts through electrene insertion, Phys. Chem. Chem. Phys. **26**, 16947 (2024).

[28] M. Naguib, M. W. Barsoum, and Y. Gogotsi, Ten years of progress in the synthesis and development of MXenes, Adv. Mater. **33**, 2103393 (2021).

[29] G. Kresse and J. Furthmiiller, Efficiency of *ab-initio* total energy calculations for metals and semiconductors using a plane-wave basis set, Comput. Mater. Sci. **6**, 15 (1996).

[30] G. Kresse and J. Furthmüller, Efficient iterative schemes for *ab initio* total-energy calculations using a plane-wave basis set, Phys. Rev. B **54**, 11169 (1996).

[31] J. P. Perdew, K. Burke, and M. Ernzerhof, Generalized gradient approximation made simple, Phys. Rev. Lett. **77**, 3865 (1996).

[32] H. J. Monkhorst and J. D. Pack, Special points for Brillouin-zone integrations, Phys. Rev. B **13**, 5188 (1976).

[33] S. Grimme, J. Antony, S. Ehrlich, and H. Krieg, A consistent and accurate *ab initio* parametrization of density functional dispersion correction (DFT-D) for the 94 elements H-Pu, J. Chem. Phys. **132**, 154104 (2010).

[34] A. Togo and I. Tanaka, First principles phonon calculations in materials science, Scr. Mater. **108**, 1 (2015).

[35] A. Togo, F. Oba, and I. Tanaka, First-principles calculations of the ferroelastic transition between rutile-type and $CaCl_2$-type SiO_2 at high pressures, Phys. Rev. B **78**, 134106 (2008).

[36] G. J. Martyna, M. L. Klein, and M. Tuckerman, Nosé–Hoover chains: The canonical ensemble via continuous dynamics, J. Chem. Phys. **97**, 2635 (1992).

[37] S. Nosé, A unified formulation of the constant temperature molecular dynamics methods, J. Chem. Phys. **81**, 511 (1984).

[38] W. Tang, E. Sanville, and G. Henkelman, A grid-based Bader analysis algorithm without lattice bias, J. Phys.: Condens. Matter **21**, 084204 (2009).

[39] See Supplemental Material at http://link.aps.org/supplemental/10.1103/PhysRevB.110.085406 for details of elastic mechanics parameters of 2D Ca_2XY_2, the mismatch of MoS_2/Ca_2Y_2 junctions; XRD patterns, phonon spectra, AIMD simulations results, Young's modulus, Poisson's ratio, ILDOS, band structures and PDOS of 2D Ca_2XY_2, projected band structures, electrostatic potential, optimized supercells, and AIMD simulations results of MoS_2/Ca_2XY_2 junctions, band structures of isolated Ca_2HfP_2_no-contact (contact), band structures and partial charge densities of isolated MoS_2_no-contact (contact), band structures of 2D Ca_2XY_2 under strain, AIMD simulations results of $MoS_2/Ca_2HfP_2/Br$ junction.

[40] J. Taylor, H. Guo, and J. Wang, *Ab initio* modeling of quantum transport properties of molecular electronic devices, Phys. Rev. B **63**, 245407 (2001).

[41] M. Büttiker, Y. Imry, R. Landauer, and S. Pinhas, Generalized many-channel conductance formula with application to small rings, Phys. Rev. B **31**, 6207 (1985).

[42] M. Y. Redko, J. E. Jackson, R. H. Huang, and J. L. Dye, Design and synthesis of a thermally stable organic electride, J. Am. Chem. Soc. **127**, 12416 (2005).

[43] S. Zhao, Z. Li, and J. Yang, Obtaining two-dimensional electron gas in free space without resorting to electron doping: An electride based design, J. Am. Chem. Soc. **136**, 13313 (2014).

[44] M. Rahm, R. Hoffmann, and N. W. Ashcroft, Atomic and ionic radii of elements 1–96, Chem. Eur. J. **22**, 14625 (2016).

[45] S. Ahmad and S. Mukherjee, A comparative study of electronic properties of bulk MoS_2 and its monolayer using DFT technique: Application of mechanical strain on MoS_2 monolayer, Graphene **03**, 52 (2014).

[46] P. Vogt, P. De Padova, C. Quaresima, J. Avila, E. Frantzeskakis, M. C. Asensio, A. Resta, B. Ealet, and G. Le Lay, Silicene: Compelling experimental evidence for graphene-like two-dimensional silicon, Phys. Rev. Lett. **108**, 155501 (2012).

[47] J. D. Mella, M. Nalabothula, F. Muñoz, K. M. Rabe, L. Wirtz, S. Singh, and A. H. Romero, Prediction of BiS_2-type pnictogen dichalcogenide monolayers for optoelectronics, npj 2D Mater. Appl. **8**, 4 (2024).

[48] J. Wang, S. Yip, S. R. Phillpot, and D. Wolf, Crystal instabilities at finite strain, Phys. Rev. Lett. **71**, 4182 (1993).

[49] K. H. Michel and B. Verberck, Theory of elastic and piezoelectric effects in two-dimensional hexagonal boron nitride, Phys. Rev. B **80**, 224301 (2009).

[50] J. S. Oh, C.-J. Kang, Y. J. Kim, S. Sinn, M. Han, Y. J. Chang, B.-G. Park, S. W. Kim, B. I. Min, H.-D. Kim *et al.*, Evidence for anionic excess electrons in a quasi-two-dimensional Ca_2N electride by angle-resolved photoemission spectroscopy, J. Am. Chem. Soc. **138**, 2496 (2016).

[51] M. Rafiee Diznab, E. R. Johnson, and J. Maassen, Periodic trends in the structural, electronic, and transport properties of electrenes, Nanoscale **15**, 12038 (2023).

[52] S. Yu, B. Huang, Y. Dai, and W. Wei, A new concept of atomically thin *p*–*n* junction based on Ca_2N/Na_2N donor–acceptor heterostructure: A first-principles study, Nanoscale **14**, 9661 (2022).

[53] S. Yu, Y. Dai, B. Huang, and W. Wei, Charge-transfer-driven phase transition of two-dimensional $MoTe_2$ in donor-acceptor heterostructures, J. Phys. Chem. Lett. **14**, 7946 (2023).

[54] B. Radisavljevic, A. Radenovic, J. Brivio, V. Giacometti, and A. Kis, Single-layer MoS_2 transistors, Nat. Nanotechnol. **6**, 147 (2011).

[55] X. Wang, S. Yu, Y. Xu, B. Huang, Y. Dai, and W. Wei, Ohmic contacts of the two-dimensional Ca_2N/MoS_2 donor–acceptor heterostructure, Phys. Chem. Chem. Phys. **25**, 15433 (2023).

[56] Y. Liu, Q. Zhang, W. Zhang, R. Zhang, B. Wang, C. Ji, Z. Pei, and S. Sang, Tuning Schottky barrier and contact type of metal–semiconductor in $Ti_3C_2T_2/MoS_2$ (T = F, O, OH) by strain: A first-principles study, J. Phys. Chem. C **125**, 16200 (2021).

[57] M. Palsgaard, T. Gunst, T. Markussen, K. S. Thygesen, and M. Brandbyge, Stacked Janus device concepts: Abrupt pn-junctions and cross-plane channels, Nano Lett. **18**, 7275 (2018).

[58] C. Jin, F. A. Rasmussen, and K. S. Thygesen, Tuning the Schottky barrier at the Graphene/MoS_2 interface by electron doping: Density functional theory and many-body calculations, J. Phys. Chem. C **119**, 19928 (2015).

[59] J. G. Simmons, Generalized formula for the electric tunnel effect between similar electrodes separated by a thin insulating film, J. Appl. Phys. **34**, 1793 (1963).

[60] N. Matthews, M. J. Hagmann, and A. Mayer, Comment: "Generalized formula for the electric tunnel effect between similar electrodes separated by a thin insulating film", J. Appl. Phys. **34**, 1793 (1963), J. Appl. Phys. **123**, 136101 (2018).

[61] Q. Wang, L. Cao, S.-J. Liang, W. Wu, G. Wang, C. H. Lee, W. L. Ong, H. Y. Yang, L. K. Ang, S. A. Yang, and Y. S. Ang, Efficient Ohmic contacts and built-in atomic sublayer protection in $MoSi_2N_4$ and WSi_2N_4 monolayers, npj 2D Mater. Appl. **5**, 71 (2021).

[62] W. Ai, Y. Shi, X. Hu, J. Yang, and L. Sun, Tunable Schottky barrier and efficient Ohmic contacts in $M Si_2N_4$ (M = Mo, W)/2D metal contacts, ACS Appl. Electron. Mater. **5**, 5606 (2023).

[63] A. Slassi, S. M. Gali, A. Pershin, A. Gali, J. Cornil, and D. Beljonne, Interlayer bonding in two-dimensional materials: The

special case of SnP_3 and GeP_3, J. Phys. Chem. Lett. **11**, 4503 (2020).

[64] X. H. Liu, J. J. Wang, C. Y. Li, Z. W. Xia, M. Jiang, and L. L. Liu, CO oxidation on graphene/Y_2C electride heterojunction, Appl. Surf. Sci. **599**, 153833 (2022).

[65] K.-A. N. Duerloo, Y. Li, and E. J. Reed, Structural phase transitions in two-dimensional Mo- and W-dichalcogenide monolayers, Nat. Commun. **5**, 4214 (2014).

[66] K. P. Dhakal, G. Ghimire, K. Chung, D. L. Duong, S. W. Kim, and J. Kim, Probing multiphased transition in bulk MoS_2 by direct electron injection, ACS Nano **13**, 14437 (2019).

[67] P. Zhao, H. Jin, X. Lv, B. Huang, Y. Ma, and Y. Dai, Modified MXene: Promising electrode materials for constructing Ohmic contacts with MoS_2 for electronic device applications, Phys. Chem. Chem. Phys. **20**, 16551 (2018).

[68] J. Wu, R. Guo, D. Wu, X. Li, and X. Wu, Turning nonmagnetic two-dimensional molybdenum disulfides into room-temperature ferromagnets by the synergistic effect of lattice stretching and charge injection, J. Phys. Chem. Lett. **15**, 2293 (2024).

[69] V. Kamysbayev, A. S. Filatov, H. C. Hu, X. Rui, F. Lagunas, D. Wang, R. F. Klie, and D. V. Talapin, Covalent surface modifications and superconductivity of two-dimensional metal carbide MXenes, Science **369**, 979 (2020).